

Research Article

Erfan Saydanzad, Jeffrey Powell, Tim Renner, Adam Summers, Daniel Rolles, Carlos Trallero-Herrero, Matthias F. Kling, Artem Rudenko and Uwe Thumm*

Generation of fast photoelectrons in strong-field emission from metal nanoparticles

<https://doi.org/10.1515/nanoph-2024-0719>

Received December 6, 2024; accepted March 24, 2025;

published online April 4, 2025

Abstract: We investigated the generation and control of fast photoelectrons (PEs) by exposing plasmonic nanoparticles (NPs) to short infrared (IR) laser pulses with peak intensities between 10^{12} and 3×10^{13} W/cm². Our measured and numerically simulated PE momentum distributions demonstrate the extent to which PE yields and cutoff energies are controlled by the NP size, material, and laser peak intensity. For strong-field photoemission from spherical silver, gold, and platinum NPs with diameters between 10 and 100 nm our results confirm and surpass extremely high PEs cutoff energies, up to several hundred times the incident laser-pulse ponderomotive energy, found recently for gold nanospheres [Saydanzad et al., *Nanophotonics* **12**, 1931 (2023)]. As reported previously for dielectric NPs [Rupp

et al., *J. Mod. Opt.* **64**, 995 (2017)], at higher intensities the cutoff energies we deduce from measured and simulated PE spectra tend to converge to a metal-independent limit. We expect these characteristics of light-induced electron emission from prototypical plasmonic metallic nanospheres to promote the understanding of the electronic dynamics in more complex plasmonic nanostructures and the design of nanoscale light-controlled plasmonic electron sources for photoelectronic devices of applied interest.

Keywords: plasmonics; nanoparticle; plasmonic-field enhancement; strong-field ionization; photoelectron imaging; electron source

1 Introduction

Photoemission from metallic nanostructures is of fundamental and practical relevance for attosecond field emission [1], [2], attosecond streaking spectroscopy of metal NPs [3], [4], efficient harmonic up-conversion [5], [6], femtosecond time-resolved scanning tunneling microscopy and spectroscopy [7]–[9], electron-impact spectroscopy [10], [11], and the development of compact electron sources [12]. Here, we demonstrate that prototypical plasmonic nanospheres, when subjected to intense IR-laser pulses, emit PEs across a broad kinetic energy spectrum, driven by a complex dynamical interplay of electronic and photonic interactions. Over the past two decades, the pronounced optical properties and plasmonic response of conduction electrons in metal NPs in the IR to visible frequency range have been extensively studied [13], [14]. The excitation of localized surface-charge plasmons (LSP) at nano-structured surfaces influences the particles' light absorption, reflection, and skin depths [15] and creates a nanoplasmonic field near the NP surface that can significantly amplify the incident laser electric field [16]–[18]. Nanoplasmonic field enhancement was predicted theoretically to importantly increase the cutoff energy in the photoionization of xenon atoms near metal NPs [19]. The LSP resonance frequency of metal NPs can be tuned from IR to visible frequencies by altering the NP shape, size, composition, and dielectric environment [13], [14], [20]–[22].

*Corresponding author: Uwe Thumm, J. R. Macdonald Laboratory, Department of Physics, Kansas State University, Manhattan, 66506, Kansas, USA, E-mail: thumm@k-state.edu.

<https://orcid.org/0000-0001-9378-6601>

Erfan Saydanzad, Daniel Rolles and Artem Rudenko, J. R. Macdonald Laboratory, Department of Physics, Kansas State University, Manhattan, 66506, Kansas, USA, E-mail: saydanzad@k-state.edu (E. Saydanzad), rolles@ksu.edu (D. Rolles), rudenko@ksu.edu (A. Rudenko).

<https://orcid.org/0000-0002-1472-5593> (E. Saydanzad)

Jeffrey Powell, J. R. Macdonald Laboratory, Department of Physics, Kansas State University, Manhattan, 66506, Kansas, USA; INRS, Énergie, Matériaux et Télécommunication, Varennes, J3X 1P7, Québec, Canada; and Department of Physics, University of Connecticut, Storrs, 06269, CT, USA, E-mail: Jeffrey.Powell@inrs.ca

Tim Renner, J. R. Macdonald Laboratory, Department of Physics, Kansas State University, Manhattan, 66506, Kansas, USA; and Department of Physics, Goethe University Frankfurt, Frankfurt am Main, 60323, Germany, E-mail: s1964921@stud.uni-frankfurt.de

Adam Summers, J. R. Macdonald Laboratory, Department of Physics, Kansas State University, Manhattan, 66506, Kansas, USA; and SLAC, National Accelerator Laboratory, Menlo Park, 94025, CA, USA, E-mail: asummers@slac.stanford.edu

Carlos Trallero-Herrero, Department of Physics, University of Connecticut, Storrs, 06269, CT, USA, E-mail: carlos.trallero@uconn.edu

Matthias F. Kling, SLAC, National Accelerator Laboratory, Menlo Park, 94025, CA, USA; and Department of Applied Physics, Stanford University, Stanford, 94305, CA, USA, E-mail: mfkling@slac.stanford.edu

This tunable enhancement of light absorption and scattering is crucial for advanced diagnostic methods, such as surface-enhanced Raman spectroscopy [23], [24], time-resolved nanoplasmonic-field microscopy [17], [25]–[27], polariton chemistry [28], and biomedical and chemical sensing [29]–[33].

In the present work, we use velocity-map-imaging (VMI) spectroscopy to investigate strong-field electron emission from metal NPs. By measuring and numerically modeling VMI spectra resulting from intense IR-laser pulses, we validate for metal NPs a recent extension [26] of the three-step model for atomic strong-field ionization [34]. VMI spectroscopy projects PE momentum distributions onto a 2-dimensional detector plane and is widely utilized to study intense-light interactions with atoms and molecules [35]–[37]. Over the past decade, this method has been used to explore strong-field photoemission from isolated NPs with intense linearly polarized laser pulses [38]–[41]. Upon emission from atoms and molecules, PEs can gain significant energy while propagating in the oscillating strong electric field of a laser pulse [42]. It is well known that for ‘direct’ emission (where the PE is not driven back to the residual ion by the external light field) from gaseous atomic targets by linearly polarized laser pulses, PEs gain up to $2U_p(I_0)$ in kinetic energy, while ‘rescattered’ PEs (that are driven back by the laser electric field to elastically scatter off the residual ion) can accumulate up to $10U_p(I_0)$ [43]–[46]. The ponderomotive energy $U_p(I_0) = I_0/(4\omega^2)$ is the cycle-averaged quiver energy of a free electron in the incident laser field of frequency ω and peak intensity I_0 . Unless otherwise stated, atomic units are used throughout this work.

For strong-field PE emission from metallic nanotips and isolated clusters, PE cutoff energies for direct and rescattered photoemission were found previously to exceed $30U_p(I_0)$ [47] and $15U_p(I_0)$ [48], respectively. Higher cutoff energies of about $50U_p(I_0)$ [40] and $140U_p(I_0)$ [22] were measured for dielectric SiO_2 and Fe_3O_4 NPs, respectively. Strong-field photoemission from isolated dielectric SiO_2 NPs by intense 25 fs 780 nm linearly polarized laser pulses was recently measured for different NP sizes and laser intensities [39]. Compared to atomic targets, strong-field emission from *metallic* plasmonic NPs was recently found experimentally [15], [49] and theoretically [26], [49] to yield the most significant enhanced PE cutoff energies of several hundred $U_p(I_0)$, due to substantial nanoplasmonic field enhancement of the incident ionizing laser pulse and a large number of emitted electrons. Caused by the strong plasmonic-near-field enhancement of the incident-laser electric field and PE correlation, the calculated cutoff energies for metal NPs

surpass those typical from gaseous atoms and dielectric NPs by two and up to one order of magnitude, respectively [26], [49].

2 Methods

2.1 Experimental setup

The experiments were carried out at the James R. Macdonald Laboratory at Kansas State University. The laser system, NP source, and VMI electron detection assembly is described in more detail in Refs. [39], [50]. Briefly, we used a Ti:Sapphire-based chirped pulse amplification (CPA) system generating 25 fs (10 optical cycles) full-width-half-intensity maximum (FWHM) pulses with a central angular frequency of $\omega = 2.354$ PHz (corresponding to a central wavelength of $\lambda = 800$ nm). The NP source consisted of an atomizer, dryer, and aerodynamic lens and injects single, isolated particles into the vacuum, where the beam of NPs intersects the focused intense laser beam [41], [50]–[53]. As depicted in the sketch of the experimental setup Figure 1, PEs generated by strong-field ionization of NPs in the laser pulse, are projected onto the detector by the static electric field between the repeller and extractor of the VMI system, allowing for the recording of the 2D projection of the PE velocity distribution. The thick-lens, high-energy VMI spectrometer is capable of detecting PEs with kinetic energies up to 350 eV [54]. The colloid NP samples with low polydispersity and high purity were purchased from Cytodiagnosics Inc. (gold and silver NPs) and Nanocomposix (platinum NPs) [55], [56].

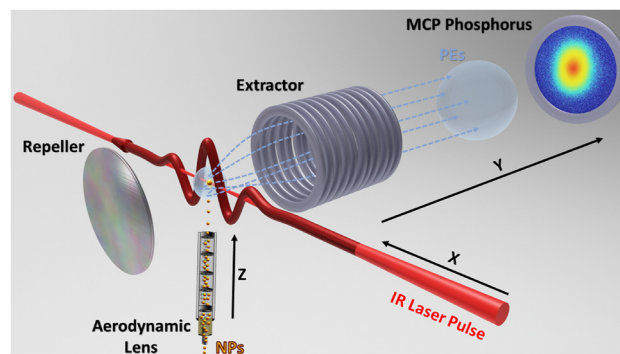


Figure 1: (Color online) Schematic of the NP source and velocity-map-imaging spectrometer setup. A beam of single, isolated NPs is injected into vacuum by an aerodynamic lens and intersects an intense linearly polarized 800 nm, 26 fs laser beam operated at a repetition-rate of 10 kHz. Emitted electrons are focused onto a microchannel plate (MCP) and phosphor assembly, from which a camera records the spatial distribution of PE hits for individual laser shots.

2.2 Laser-intensity characterization

For the laser intensity and PE momentum calibration, we employed the VMI spectrometer described above to measure above-threshold-ionization (ATI) PE momentum distributions from gaseous Xe atoms [57]. This measurement was done under the same experimental conditions as for the photoemission-from-NP experiments reported here. From the 2D projection of the PE momentum distributions, we determined the ponderomotive shift of the ATI combs. Based on the proportionality of the ponderomotive energy and peak intensity of the incident laser pulse, I_0 , we determined the intensities used in this work in the interval $10^{12} \text{ W/cm}^2 < I_0 < 3 \times 10^{13} \text{ W/cm}^2$. We estimated the accuracy of the intensity calibration to be better than 15 % [50], [58].

2.3 Theoretical model

The high laser intensities we consider generate multiply ionized NPs [39], [51]. We numerically model PE emission from metallic NPs by IR-laser pulses with a Gaussian temporal profile. Propagating along the x axis and linearly polarized along the z axis, their electric field is given by

$$\vec{E}_{inc}(\vec{r}, t) = \sqrt{I_0} \exp\left[-2 \ln 2 \frac{(t - x/c)^2}{\tau^2}\right] \times \exp[-i\omega(t - x/c) + i\psi] \hat{e}_z, \quad (1)$$

where τ is the pulse length at FWHM, ω the pulses' central frequency, ψ the carrier-envelope phase, and c the speed of light in vacuum (Figure 1). During the laser - NP interaction, LSPs are excited and induce an inhomogeneous plasmonic field near the NP surface. Most significantly at the LSP resonance frequency [59], [60], electrons are excited to electronic states above the Fermi level. Sufficiently high laser intensities generate multiply ionized NPs [39], [51]. The incident laser pulse thus transiently polarizes the NP. Within the electric-dipole approximation, the corresponding transient induced plasmonic dipole moment, $\vec{P}_{pl}(t) = \epsilon_0 \alpha_{Mie}(\omega) \vec{E}_{inc}(\vec{r}, t)$, gives raise to the plasmonic electric field [61]

$$\vec{E}_{pl}(\vec{r}, t) = \frac{e^{ikr}}{r} \left\{ k^2 \left[\hat{e}_r \times \vec{P}_{pl}(t) \right] \times \hat{e}_r + \left[3\hat{e}_r \left[\hat{e}_r \cdot \vec{P}_{pl}(t) \right] - \vec{P}_{pl}(t) \right] \left(\frac{1}{r^2} - \frac{ik}{r} \right) \right\}, \quad (2)$$

where $k = 2\pi/\lambda = \omega/c$. We calculate the complex NP polarizability, $\alpha_{Mie}(\omega)$, within Mie theory [62], [63], which restricts the applicability of Eq. (2) for nanospheres of radius a to size parameters $ka \lesssim 0.6$ [64].

We describe strong-field ionization from metal NPs by extending the semi-classical three-step model (also known as the 'simple-man model') for atomic strong-field ionization to metal NPs [26]. Our extended three-step model consists of (1) electron release based on quantum-mechanical tunneling, (2) PE propagation from the NP surface to the detector by sampling over classical trajectories, and (3) PE rescattering and recombination at the NP surface. In comparison with gaseous atomic targets, each of these steps is significantly more intricate for metal NPs. This is due to the NPs' more complex electronic structure, the added morphological structure, and the emission of a much larger number of electrons compounding the effects of PE - PE correlation, residual charges, and PE - nanoplasmonic-field interactions.

We represent the NPs' static electronic structure in terms of the surface potential step $V_0 = \epsilon_F + \varphi$, given by the work function φ and Fermi energy ϵ_F for bulk metal [65]. During successive small time intervals, our dynamical numerical simulation divides the NP surface into small surface elements, which are modeled as square-well potentials. Bound PEs close to the NP surface are assumed to tunnel out in radial direction, driven by the radial component of the total electric field at the NP surface, $\vec{F} \cdot \hat{e}_r$, where $\vec{F} = \vec{E}_{inc} + \vec{E}_{pl} + \vec{F}_{res}$. The residual-charge field \vec{F}_{res} results from the accumulation of positive residual charge on the NP during electron emission in preceding time intervals. We account for strong-field electron release from the NP by employing modified [26] Fowler-Nordheim tunneling rates [66]. Subsequently, we Monte Carlo sample over the initial phase-space distribution of released electrons and solve Newton's equations of motion for the PE propagation outside the NP in the presence of all electric fields, $\vec{F} + \vec{F}_{e-e}$, where \vec{F}_{e-e} is the repulsive Coulomb electric field between PEs. In each laser half-cycle the direction of the incident-laser electric field changes, such that emitted PEs can be accelerated back toward the NP and either rescatter from or recombine at the NP surface. We include and numerically evaluate the effects of PE repulsion, residual positive charges on the NP, PE recollisions and recombinations at the NP surface, and nanoplasmonic enhancement of the incident-laser-pulse electric field. More details about the numerical model are given in Ref. [26] and the Supplementary Information of Ref. [49].

3 Experimental and simulation results

3.1 Photoelectron-momentum images

We start the presentation of our results with a comparison of laser-intensity and size-dependent measured and

numerically simulated PE spectra for silver, gold, and platinum nanospheres. Figures 2, 3, and S1 display simulated and experimental VMI spectra for silver nanospheres with diameters of 10, 60, and 100 nm, respectively. The first, second, and third columns present simulated VMI spectra for the direct, rescattered, and net PE yields. The rows represent results for different peak laser intensities I_0 . Our numerical results in the third column are compared with our measured VMI spectra, shown in the fourth column for the three highest intensities. To facilitate a quantitative comparison between the direct and rescattered PE yields, we normalized the yields in each row to the corresponding net PE yield in the third column and display normalized integrated yields μ in all graphs.

For comparison with the simulated VMI spectra for silver NPs in Figures 2, 3, and S1, we provide in Figures S2, S3, and S4 of the Supplementary Information (SI) corresponding calculated spectra for gold NPs of identical diameter for the same peak intensities. Additional measured and simulated VMI spectra for gold NPs with different diameters and for other laser intensities than in the present work can be

found in Ref. [49]. Figures S5 and S6 in the SI show a comparison of simulated and experimental VMI spectra for gold and platinum NPs with a diameter of 70 nm, respectively. For the examined transition metals, all simulated VMI spectra exhibit a slight elongation along the laser polarization direction, with PE cutoff energies and yields increasing with NP size and laser intensity. The high degree of isotropy is a direct result of the Coulomb repulsion between PEs and diffuse PE rescattering from the NP surface, as discussed for gold NPs in [26], [49].

We expect the yield parameter μ for rescattered PEs to consistently increase with both NP size and laser intensity: Higher laser intensities result in enhanced PE emission from the NP surface and higher residual charge accumulation on the NP. The accumulated residual charge enhances the yield of rescattered PEs. An increase in NP size provides a larger surface area for the laser - NP interaction, leading to increased PE emission and, consequently, enhanced PE rescattering. This effect is somewhat mitigated at larger sizes due to the, on average, larger distance between emitted PEs and accumulated residual charges.

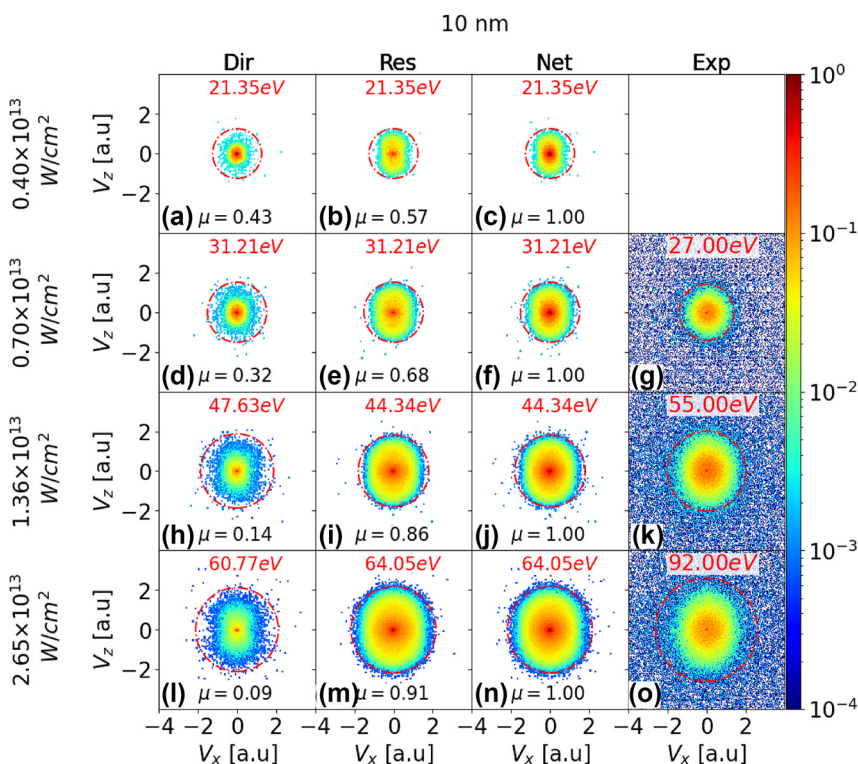


Figure 2: VMI PE spectra for strong-field ionization of silver nanospheres with 10 nm diameter and laser peak intensities of 4.0×10^{12} , 7.0×10^{12} , 1.36×10^{13} , and 2.65×10^{13} W/cm² (first - fourth row, respectively). Comparison of simulated direct (first column), rescattered (second column), and net (direct plus rescattered yields, third column) spectra with experimental spectra (fourth column). The laser-pulse length and wavelength are 25 fs FWHM and 800 nm, respectively. In each row, calculated integrated PE yields for direct and rescattered emission, μ , are normalized to the integrated net yields in the third column. The red circle in each VMI map represents the photoemission cutoff. The cutoff energies are given in red above the VMI maps. No experimental data is available for 4.0×10^{12} W/cm² peak intensity.

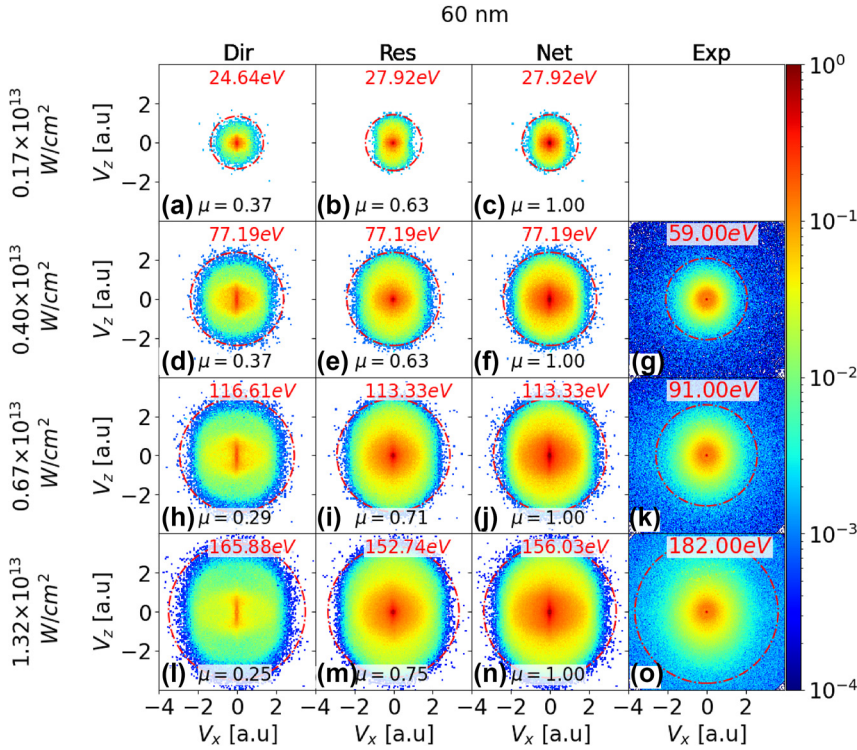


Figure 3: As Figure 2 for 60 nm diameter silver nanoparticles and laser peak intensities of 1.7×10^{12} , 4.0×10^{12} , 6.7×10^{12} , and 1.32×10^{13} W/cm² (first – fourth row, respectively).

The increase in yield with both NP size and intensity is nonlinear. An increasing residual charge on the NP tends to impede electron emission and, thus, to slow the growth of the electron yield with increasing laser intensity. This effect is comparable to the increase of the residual charge and work function of fullerene clusters during sequential electron capture by slow highly charged ionic projectiles [67]–[69]. Below, we shall refer to this observation as ‘*yield-saturation effect*’. It occurs with increasing laser intensity I_0 at larger PE yields. We hold the underlying electronic dynamics accountable for the complex change of the branching ratio between direct and rescattered PE yields as a function of the laser intensity and NP size (cf., Figures 2, 3, S1, and S1).

At low intensities, the yield of rescattered PE increases relative to the direct-emission yield with the NP size, as is seen by comparing, e.g., Figures 2b and 3b. This yield increase is compatible with the larger effective surface area (geometrical cross section) for laser – NP interactions and electron rescattering. Consequently, an increase in NP size leads to higher PE yields and promotes rescattering. In contrast, the rescattering yield decreases for increasing NP size relative to direct emission at high intensities, as is illustrated by comparing, e.g., Figure 2(i) and 3(i) or Figure 2(m) and

3(m) for silver NPs. This indicates that now, at high intensity, the increase of the geometrical rescattering cross is less competitive in promoting rescattering over direct emission. The relative smaller chance for rescattering is compatible with the lower rate of residual-charge accumulation that is also deemed responsible for the yield-saturation (cf. Figure 5).

3.2 Cutoff energies and net PE yields

In this subsection we discuss laser-intensity and NP-size dependent PE cutoff energies and total yields for silver, gold, and platinum nanoparticles. Extended exposure to the laser electric field leads to rescattering as the dominant mechanism for reaching the highest observable PE kinetic energies. The PE cutoff energy E_{cutoff}^R is thus determined by rescattered PEs (denoted by the superscript ‘*R*’). The effects of PE Coulomb repulsion, PE attraction by the built-up residual positive charge of the NP, and plasmonic field enhancement on E_{cutoff}^R can be represented by the heuristic formula [49].

$$E_{\text{cutoff}}^R = 10 U_p(I_0) [\eta_{\text{eff}}^R(a, I_0) + \omega t_f \eta_C^R(a, I_0)]^2. \quad (3)$$

This expression describes the influence on photoemission of the plasmonic field enhancement near the NP in terms of the

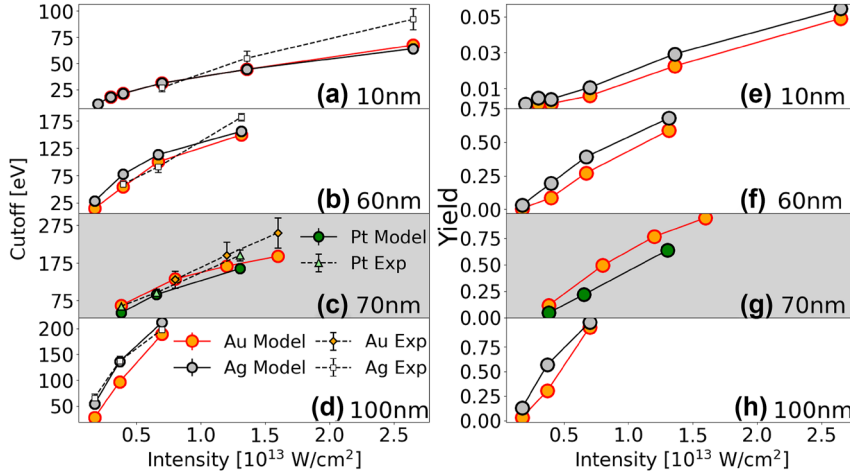


Figure 4: Simulated and experimental PE cutoff energies (a–d) and simulated yields (e–h) for gold, silver, and platinum nanoparticles. (a,b,d,e,f,h) show PE cutoff energies and yields for gold and silver nanoparticles with diameters of 10, 60, and 100 nm. (c,g) display PE cutoff energies and yields for gold and platinum nanoparticles with a diameter of 70 nm. The gold – platinum comparisons is plotted against a gray background, for better distinction from the silver – gold results.

averaged enhancement factor $\eta_{\text{eff}}^R(a, I_0) < \eta(a, I_0)$ [64]. The effective enhancement factor η_{eff}^R is expected to be smaller than the plasmonic field enhancement $\eta(a, I_0)$ due to the decreasing strength of the nanoplasmonic field for increasing polar angles and PE-distances and due to averaging over the PE dynamics. Repulsive PE – PE and attractive PE – residual-charge Coulomb interactions are represented within a simplified central-field picture, respectively, as the contributions $\eta_{e-e}^R(a, I_0) > 0$ and $\eta_{\text{res}}^R(a, I_0) > 0$ to the effective Coulomb interaction factor

$$\eta_C^R(a, I_0) = \eta_{e-e}^R(a, I_0) - \eta_{\text{res}}^R(a, I_0). \quad (4)$$

Our measured large cut-off energies indicate PE – PE interactions to dominate over PE – residual charge interactions for all intensities and sizes, such that $\eta_C^R(a, I_0) > 0$. For the laser parameters used in this study, the effective interaction time is determined at numerical convergence as $\omega t_f = 120.75 \approx 2\omega\tau$. Equation (3) and Table 1 explain qualitatively our experimental and simulated results in Figure 4 in terms of material characteristics and the NP size. The PE yield and cutoff energy tend to increase with decreasing work

Table 1: Work function φ and calculated plasmonic field enhancement η for gold, silver, and platinum nanoparticles of diameter $2a$. The listed work functions are bulk values.

Material	$2a$ [nm]	φ [eV]	η
Gold	10, 60, 70, 100	5.10	3.27, 3.42, 3.47, 3.65
Silver	10, 60, 100	4.26	3.23, 3.37, 3.59
Platinum	70	5.65	3.26

function, increasing plasmonic field enhancement, and increasing NP diameter [26], [49]. The leading factor $U_p(I_0)$ in Eq. (3) is linear in the laser peak intensity I_0 . We further note that the magnitude of the linear shift of the peak position in ATI spectra measured from sharp metal tips [70] was previously attributed to the plasmonic field enhancement of the incident IR pulse [71], in support of the evidence we find for strong plasmonic effects on photoemission from metal NPs.

Figures 4a, b, and d present measured and simulated PE cutoff energies for gold and silver nanoparticles. Figure 4c shows PE cutoff energies for platinum nanoparticles with a diameter of 70 nm. We numerically simulated cutoff energies as the energy up to which 99.5 % of the net PE yield has accumulated [26], [49]. The experimental cutoff energies were extracted from the VMI maps as described in more detail in Refs. [39], [50].

Although experimental and simulated values are comparable in magnitude and show the same general trends in their size and intensity dependence, their overall agreement in Figure 4 is not perfect. We attribute the remaining discrepancies in part to the following uncertainties: With regard to the numerical simulation, a serious uncertainty derives from our implementation of approximate modified Fowler–Nordheim tunneling rates. While our simulated spectra are background-free and not adjusted for the experimental spectral detection efficiency, both background yields and detection uncertainties affect the measured data. The measured PE yields are subject to focal-volume averaging, such that for a given laser peak intensity, NPs exposed to a large range of intensities contribute to the PE yield.

We partially offset this focal-volume effect by generating histograms of the number of PEs emitted per laser shot versus the number of laser shots. We then selected for our data analysis laser shots that yield the largest numbers of detected PEs, assuming they have illuminated NPs with intensities close to the laser peak intensity I_0 . PE counts associated with these preselected shots were added to compose the VMI maps shown in this work. From these maps the cutoff energies were defined where the PE yield becomes indistinguishable from the background [39], [50]. Other effects contributing to the measurement error in PE yields and energies are related to the (i) predominant emission of slow electrons overexposing the center of our MCP detector for the larger NPs and higher peak intensities used in the present work, (ii) NPs deviating from the ideal spherical shape and nominal size, and (iii) NP surfaces being coated with residual chemicals. Due to detection inefficiencies, the recorded PE yield is smaller than the actual yield. This difference is more significant for larger NPs and higher laser peak intensities.

Simulated PE yields for the NP materials and sizes in Figures 4a–d are shown in Figures 4e–h, respectively. For the laser parameters and targets in this study, comparing different materials of equal size shows that plasmonic field enhancements vary slightly for the considered metals (Table 1). PE yields and cutoff energies are larger for smaller work functions. In general, for high PE yield, the second term in Eq. (3) dominates, leading to larger cutoff energies. However, for the low PE yield in Figure 4(e), the second term in Eq. (3) becomes negligible and plasmonic enhancement dominates. Since the plasmonic field enhancement is slightly larger for gold than for silver, the cutoff energy is slightly higher for gold than for silver, especially at high intensities.

Figure 5 compares the simulated and experimental cutoff energies in Figure 4, scaled by the incident-laser ponderomotive energy $U_p(I_0)$. The error bars for the scaled cutoff energy are interpolated and shown as light- and dark-colored bands. They are calculated as

$$\Delta E_{U_p} = \left| \frac{\Delta E_{eV}}{U_p} \right| + E_{U_p} \left| \frac{\Delta I_0}{I_0} \right|, \quad (5)$$

where ΔE_{eV} represents the uncertainty in the cutoff energy in units of eV. The light shaded regions in Figure 5 correspond to the error range given by the first term in Eq. (5), representing the uncertainty in the U_p -scaled cutoff energy. The darker shaded regions additionally account for a 10% uncertainty in the laser peak intensity, as described by the second term in Eq. (5). This conservatively assumed accuracy of 10% is of the order of the estimated intensity accuracy in our experiment (cf., Section 2.2) and clearly

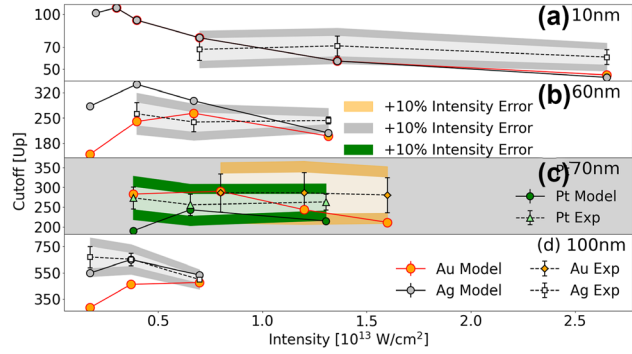


Figure 5: Simulated and experimental PE cutoff energies in Figures 4a–d in units of the incident-laser ponderomotive energy $U_p(I_0) \sim I_0$.

exceeds the typical calibration standard for laser peak intensities of 1.3% [72]. The lighter regions exclude this intensity-related uncertainty.

In striking contrast to atomic targets, cutoff energies for NPs are significantly higher and exhibit a nonlinear dependence on the laser peak intensity I_0 . U_p -scaled cutoffs reach maxima that vary with the size and composition of the NPs. The emission saturation effect discussed in Section 3.1 occurs with increasing laser peak intensity I_0 . At low laser peak intensity and far from the above-introduced emission saturation intensity, increasing the laser peak intensity leads to a rapid increase in yield and, consequently, an increase in the cutoff energies in Figures 4 and 5. In contrast, at high laser peak intensity and close to the emission saturation intensity, a further increase in the intensity results in a slow yield increase and, consequently, an increase in the cutoff energy in units of eV in Figure 4 and decreasing U_p -scaled cutoffs in Figure 5.

For the considered transition metals and NPs of the same size, the simulated cutoff energies tend to converge to the same value at laser high intensity. The reason for this behavior is that – at high intensities – differences in the relevant material properties, i.e., different dielectric responses (resulting in material dependent plasmonic field enhancements) and different work functions (accounting for different net PE yields), become negligible, since these intensities are very close to the emission saturation intensity. In other words, at such high intensities, residual-charge and repulsive-Coulomb interactions between a large number of PEs become the primary elementary interactions that determine the shape of the PE spectrum at high PE energies and thus the cutoff energy.

A similar convergence to intensity-independent cutoff energies was observed for dielectric NPs [22]. The authors' numerical simulations show a decreasing intensity and material dependence of the U_p -scaled cutoff energy due to

dominant many-particle interactions, similar to our finding, albeit at larger laser intensities. The onset of this saturation effect occurring at larger intensities for dielectric, as compared to metal, NPs is expected, since higher field strengths are required for dielectric materials to release sufficiently many electrons for generating overwhelming PE Coulomb interactions.

In view of the PE spectra and cutoff energies discussed in this work being determined by complex strong-field driven many-electron interactions [26], the main characteristics in our measured spectra and cutoff energies and trends in their dependence on the NP size and laser intensity are reasonably well reproduced by our numerical simulation, while some discrepancies remain. An important uncertainty in our simulation derives from our use of modified Fowler-Nordheim tunneling rates [26], as mentioned above. A more realistic account of electron tunneling at the NP surface, possibly based on density-functional theory, will likely be a key improvement for simulating more accurate PE yields. Expanding on the discussion of experimental errors given above in relation to the cutoff energies in Figure 4, we note that detector saturation decreases the reliability of the low-energy portion of our spectra. While this portion of the simulation data was truncated to allow for a better comparison with the experiment, the detection uncertainty due to saturation is not completely removed and tends to affect predominantly measurements with the largest NPs and highest laser peak intensity presented in this work, due to larger numbers of emitted PE per laser shot [49]. Furthermore, the unequal PE yield for different NP sizes imposed a practical limit on the laser intensities. Small 10 nm NPs produce a much smaller PE yield than 100 nm NPs. We therefore increased the laser intensity for the small particles, as the signal for the lowest intensity was insufficient to generate reliable VMI spectra for the determination of cutoff energies. In contrast, for the larger particles, our larger intensities saturate the MCP, rendering the recorded VMI spectra useless for determining cutoff energies. These experimental constraints lead to the seemingly large range of, in part unequal, intensities we selected for different nanoparticle sizes.

4 Conclusions

We measured and numerically simulated angle- and energy-resolved PE spectra for strong-field ionization from prototypical plasmonic metal nanospheres. Our experimental and simulated results reveal a complex interplay of PE emission, propagation, recombination, and rescattering.

Enhanced by strong plasmonic fields, a substantial number of PEs tunnel-ionize from metal NPs, resulting in high PE yields and cutoff energies. We analyzed the dependence of PE angular distributions, yields, and cutoff energies on material type, NP size, and laser intensity for direct and rescattered photoemission. Our findings for three transition metals indicate that metal NPs are effective sources for generating high-energy PEs, with their yield and energy being tunable through target properties such as size and material type, as well as by adjusting the laser wavelength and peak intensity. In analogy to the behavior of PE cutoff energies for strong-field emission from dielectric NPs [22], at higher intensities our measured and simulated PE cutoff energies tend to converge to a metal-independent limit. Our results show that the work function, plasmonic field enhancement, and size are crucial determinants for strong-field photoemission from NPs. At high laser peak intensities, our numerical model further predicts the PE yield and cutoff energy to saturate due to the accumulation of residual charge on the NP surface.

Research funding: JP and CT were supported by the Air Force Office of Scientific Research award no. FA9550-17-1-0369 and FA9550-21-1-0387 (Recollision physics at the nanoscale). TR acknowledges support for a summer internship at KSU through the DAAD RISE program. UT was supported by NSF grant PHY 2409183 (Strong-field emission and nonlinear response of nanoparticles). ES, AR and DR acknowledge support by the Chemical Sciences, Geosciences, and Biosciences Division, Office of Basic Energy Sciences, Office of Science, U.S. DOE under award No. DEFG02-86ER13491. AS and MFK were supported by the U.S. Department of Energy, Office of Science, Basic Energy Sciences, Scientific User Facilities Division, under Contract No. DE-AC02-76SF00515. MFK acknowledges partial support of his effort in the interpretation of the data by the Chemical Sciences, Geosciences, and Biosciences Division, Office of Basic Energy Sciences, Office of Science, US DOE.

Author contributions: All authors have accepted responsibility for the entire content of this manuscript and consented to its submission to the journal, reviewed all the results and approved the final version of the manuscript. The experiments were performed by JP, AS, DR, CTH, MFK, and AR. The numerical simulations were done by ES, TR, and UT.

Conflict of interest: Authors state no conflicts of interest.

Informed consent: Informed consent was obtained from all individuals included in this study.

Ethical approval: The conducted research is not related to either human or animals use.

Data availability: All experimental raw data and simulation results are stored electronically at Kansas State University and will be available upon reasonable request.

References

- [1] H. Y. Kim, M. Garg, S. Mandal, L. Seiffert, T. Fennel, and E. Goulielmakis, “Attosecond field emission,” *Nature*, vol. 613, no. 7945, pp. 662–666, 2023.
- [2] P. Dienstbier, *et al.*, “Tracing attosecond electron emission from a nanometric metal tip,” *Nature*, vol. 616, no. 7958, pp. 702–706, 2023.
- [3] E. Saydanzad, J. Li, and U. Thumm, “Spatiotemporal imaging of plasmonic fields near nanoparticles below the diffraction limit,” *Phys. Rev. A*, vol. 98, no. 6, p. 063422, 2018.
- [4] J. Li, E. Saydanzad, and U. Thumm, “Imaging plasmonic fields with atomic spatiotemporal resolution,” *Phys. Rev. Lett.*, vol. 120, no. 22, p. 223903, 2018.
- [5] C. Winterfeldt, C. Spielmann, and G. Gerber, “Colloquium: optimal control of high-harmonic generation,” *Rev. Mod. Phys.*, vol. 80, no. 1, p. 117, 2008.
- [6] S. Ghimire and D. A. Reis, “High-harmonic generation from solids,” *Nat. Phys.*, vol. 15, no. 1, pp. 10–16, 2019.
- [7] M. Dabrowski, Y. Dai, and H. Petek, “Ultrafast photoemission electron microscopy: imaging plasmons in space and time,” *Chem. Rev.*, vol. 120, no. 13, pp. 6247–6287, 2020.
- [8] M. Müller, V. Kravtsov, A. Paarmann, M. B. Raschke, and R. Ernstorfer, “Nanofocused plasmon-driven sub-10 fs electron point source,” *ACS Photonics*, vol. 3, no. 4, pp. 611–619, 2016.
- [9] S. Yoshida, *et al.*, “Terahertz scanning tunneling microscopy for visualizing ultrafast electron motion in nanoscale potential variations,” *ACS Photonics*, vol. 8, no. 1, pp. 315–323, 2021.
- [10] K. N. Walzl, C. F. Koerting, and A. Kuppermann, “Electron-impact spectroscopy of acetaldehyde,” *J. Chem. Phys.*, vol. 87, no. 7, pp. 3796–3803, 1987.
- [11] K. Venkatraman, B. D. A. Levin, K. March, P. Rez, and P. A. Crozier, “Vibrational spectroscopy at atomic resolution with electron impact scattering,” *Nat. Phys.*, vol. 15, no. 12, pp. 1237–1241, 2019.
- [12] J. Schötz, *et al.*, “Onset of charge interaction in strong-field photoemission from nanometric needle tips,” *Nanophotonics*, vol. 10, no. 14, pp. 3769–3775, 2021.
- [13] K. Lance Kelly, E. Coronado, L. Z. Lin, and G. C. Schatz, “The optical properties of metal nanoparticles: the influence of size, shape, and dielectric environment,” *J. Phys. Chem. B*, vol. 107, no. 3, pp. 668–677, 2003.
- [14] Lu Wang, M. Hasanzadeh Kafshgari, and M. Meunier, “Optical properties and applications of plasmonic-metal nanoparticles,” *Adv. Funct. Mater.*, vol. 30, no. 51, p. 2005400, 2020.
- [15] J. A. Powell, *et al.*, “Strong-field control of plasmonic properties in core–shell nanoparticles,” *ACS Photonics*, vol. 9, no. 11, pp. 3515–3521, 2022.
- [16] M. I. S. Nanoplasmonics, “The physics behind the applications,” *Physics Today*, vol. 64, no. 29, 2011.
- [17] J. Li, E. Saydanzad, and U. Thumm, “Attosecond time-resolved streaked photoelectron spectroscopy of transition-metal nanospheres,” *Phys. Rev. A*, vol. 95, no. 2, p. 043423, 2017.
- [18] M. F. Ciappina, *et al.*, “Attosecond physics at the nanoscale,” *Rep. Prog. Phys.*, vol. 80, no. 5, p. 054401, 2017.
- [19] M. F. Ciappina, *et al.*, “High energy photoelectron emission from gases using plasmonic enhanced near-fields,” *Laser Phys. Lett.*, vol. 10, no. 10, p. 105302, 2013.
- [20] S. Link and M. A. El-Sayed, “Size and temperature dependence of the plasmon absorption of colloidal gold nanoparticles,” *J. Phys. Chem. B*, vol. 103, no. 21, pp. 4212–4217, 1999.
- [21] P. K. Jain, X. Huang, I. H. El-Sayed, and M. A. El-Sayed, “Review of some interesting surface plasmon resonance-enhanced properties of noble metal nanoparticles and their applications to biosystems,” *Plasmonics*, vol. 2, no. 3, pp. 107–118, 2007.
- [22] P. Rupp, *et al.*, “Quenching of material dependence in few-cycle driven electron acceleration from nanoparticles under many-particle charge interaction,” *J. Mod. Opt.*, vol. 64, nos. 10–11, pp. 995–1003, 2017.
- [23] E. Le Ru and P. Etchegoin, *Principles of Surface-Enhanced Raman Spectroscopy: And Related Plasmonic Effects*, Oxford, Elsevier, 2008.
- [24] V. Cupil-Garcia, *et al.*, “Plasmonic nanoplatforms: from surface-enhanced Raman scattering sensing to biomedical applications,” *J. Raman Spectrosc.*, vol. 52, no. 2, pp. 541–553, 2021.
- [25] M. I. Stockman, M. F. Kling, U. Kleineberg, and F. Krausz, “Attosecond nanoplasmonic-field microscope,” *Nat. Photonics*, vol. 1, no. 9, pp. 539–544, 2007.
- [26] E. Saydanzad, J. Li, and U. Thumm, “Strong-field ionization of plasmonic nanoparticles,” *Phys. Rev. A*, vol. 106, no. 3, p. 033103, 2022.
- [27] J. Li, E. Saydanzad, and U. Thumm, “Retrieving plasmonic near-field information: a quantum-mechanical model for streaking photoelectron spectroscopy of gold nanospheres,” *Phys. Rev. A*, vol. 94, no. 5, p. 051401, 2016.
- [28] A. Mandal, M. A. D. Taylor, B. M. Weight, E. R. Koessler, X. Li, and P. Huo, “Theoretical advances in polariton chemistry and molecular cavity quantum electrodynamics,” *Chem. Rev.*, vol. 123, no. 16, pp. 9786–9879, 2023.
- [29] L. Song, J. Chen, B. B. Xu, and Y. Huang, “Flexible plasmonic biosensors for healthcare monitoring: progress and prospects,” *ACS Nano*, vol. 15, no. 12, pp. 18822–18847, 2021.
- [30] C. Lee, B. Lawrie, R. Pooser, K.-G. Lee, C. Rockstuhl, and M. Tame, “Quantum plasmonic sensors,” *Chem. Rev.*, vol. 121, no. 8, pp. 4743–4804, 2021.
- [31] A. V. Kabashin, *et al.*, “Plasmonic nanorod metamaterials for biosensing,” *Nat. Mater.*, vol. 8, no. 11, p. 867, 2009.
- [32] K. A. Willets and R. P. Van Duyne, “Localized surface plasmon resonance spectroscopy and sensing,” *Annu. Rev. Phys. Chem.*, vol. 58, no. 1, pp. 267–297, 2007.
- [33] V. Montes-García, M. A. Squillaci, M. Diez-Castellnou, Q. K. Ong, F. Stellacci, and P. Samori, “Chemical sensing with Au and Ag nanoparticles,” *Chem. Soc. Rev.*, vol. 50, no. 2, pp. 1269–1304, 2021.
- [34] P. B. Corkum, “Plasma perspective on strong field multiphoton ionization,” *Phys. Rev. Lett.*, vol. 71, no. 13, pp. 1994–1997, 1993.
- [35] J. Maurer, D. Dimitrovski, L. Christensen, L. B. Madsen, and H. Stapelfeldt, “Molecular-frame 3d photoelectron momentum distributions by tomographic reconstruction,” *Phys. Rev. Lett.*, vol. 109, no. 12, p. 123001, 2012.
- [36] H. V. Sa Lam, T. N. Wangjam, and V. Kumarappan, “Alignment dependence of photoelectron angular distributions in the few-photon ionization of molecules by ultraviolet pulses,” *Phys. Rev. A*, vol. 105, no. 5, p. 053109, 2022.

- [37] M. Meckel, *et al.*, “Laser-induced electron tunneling and diffraction,” *Science*, vol. 320, no. 5882, pp. 1478–1482, 2008.
- [38] V. Leshchenko, A. Camacho Garibay, B. Smith, P. Agostini, and L. F. DiMauro, “Universal scaling laws in nanoplasmonics of laser-ionized nanospheres,” *Phys. Rev. A*, vol. 110, no. 1, p. 013117, 2024.
- [39] J. A. Powell, *et al.*, “Interplay of pulse duration, peak intensity, and particle size in laser-driven electron emission from silica nanospheres,” *Opt. Express*, vol. 27, no. 19, pp. 27124–27135, 2019.
- [40] S. Zherebtsov, *et al.*, “Controlled near-field enhanced electron acceleration from dielectric nanospheres with intense few-cycle laser fields,” *Nat. Phys.*, vol. 7, no. 8, pp. 656–662, 2011.
- [41] L. Seiffert, *et al.*, “Attosecond chronoscopy of electron scattering in dielectric nanoparticles,” *Nat. Phys.*, vol. 13, no. 8, p. 766, 2017.
- [42] K. Lv, “Ionization in the field of a strong electromagnetic wave,” *Sov. Phys. JETP*, vol. 20, no. 5, pp. 1307–1314, 1965.
- [43] G. G. Paulus, W. Becker, W. Nicklich, and H. Walther, “Rescattering effects in above-threshold ionization: a classical model,” *J. Phys. B: At., Mol. Opt. Phys.*, vol. 27, no. 21, p. L703, 1994.
- [44] B. Walker, B. Sheehy, K. C. Kulander, and L. F. DiMauro, “Elastic rescattering in the strong field tunneling limit,” *Phys. Rev. Lett.*, vol. 77, no. 25, p. 5031, 1996.
- [45] W. Becker, F. Grasbon, R. Kopold, D. B. Milošević, G. G. Paulus, and H. Walther, “Above-threshold ionization: from classical features to quantum effects,” in *Advances in Atomic, molecular, and optical physics*, vol. 48, Amsterdam, Elsevier, 2002, pp. 35–98.
- [46] W. Becker, S. P. Goreslavski, D. B. Milošević, and G. G. Paulus, “The plateau in above-threshold ionization: the keystone of rescattering physics,” *J. Phys. B*, vol. 51, no. 16, p. 162002, 2018.
- [47] H. Yanagisawa, *et al.*, “Delayed electron emission in strong-field driven tunnelling from a metallic nanotip in the multi-electron regime,” *Sci. Rep.*, vol. 6, no. 1, p. 35877, 2016.
- [48] Z. Wang, *et al.*, “Universal high-energy photoelectron emission from nanoclusters beyond the atomic limit,” *Phys. Rev. Lett.*, vol. 124, no. 17, p. 173201, 2020.
- [49] E. Saydanzad, *et al.*, “Enhanced cutoff energies for direct and rescattered strong-field photoelectron emission of plasmonic nanoparticles,” *Nanophotonics*, vol. 12, no. 10, pp. 1931–1942, 2023.
- [50] J. A. Powell, “Strong-field driven dynamics of metal and dielectric nanoparticles,” Ph.D. thesis, Kansas State University, Manhattan, 2017.
- [51] F. Süßmann, *et al.*, “Field propagation-induced directionality of carrier-envelope phase-controlled photoemission from nanospheres,” *Nat. Commun.*, vol. 6, no. 1, p. 7944, 2015.
- [52] J. L. Ellis, *et al.*, “Materials properties and solvated electron dynamics of isolated nanoparticles and nanodroplets probed with ultrafast extreme ultraviolet beams,” *J. Phys. Chem. Lett.*, vol. 7, no. 4, pp. 609–615, 2016.
- [53] M. Davino, T. Saule, N. G. Helming, J. A. Powell, and C. Trallero-Herrero, “Characterization of an aerosolized nanoparticle beam beyond the diffraction limit through strong field ionization,” *Sci. Rep.*, vol. 12, no. 1, p. 9277, 2022.
- [54] N. Kling, *et al.*, “Thick-lens velocity-map imaging spectrometer with high resolution for high-energy charged particles,” *J. Instrum.*, vol. 9, no. 5, p. P05005, 2014.
- [55] We purchased the nanoparticles from Cytodiagnosics inc. <https://www.cytodiagnosics.com>.
- [56] P. Rosenberger, *et al.*, “Near-field induced reaction yields from nanoparticle clusters,” *ACS Photonics*, vol. 7, no. 7, pp. 1885–1892, 2020.
- [57] P. Agostini, F. Fabre, G. Mainfray, G. Petite, and N. K. Rahman, “Free-free transitions following six-photon ionization of xenon atoms,” *Phys. Rev. Lett.*, vol. 42, no. 17, pp. 1127–1130, 1979.
- [58] A. M. Summers, “Strong-field interactions in atoms and nanosystems: advances in fundamental science and technological capabilities of ultrafast sources,” PhD thesis, Kansas State University, Manhattan, 2019.
- [59] C. S. Kumarasinghe, M. Premaratne, Q. Bao, and G. P. Agrawal, “Theoretical analysis of hot electron dynamics in nanorods,” *Sci. Rep.*, vol. 5, no. 1, p. 12140, 2015.
- [60] P. Narang, R. Sundararaman, and H. A. Atwater, “Plasmonic hot carrier dynamics in solid-state and chemical systems for energy conversion,” *Nanophotonics*, vol. 5, no. 1, pp. 96–111, 2016.
- [61] J. D. Jackson, *Classical electrodynamics*, 3rd ed., New York, Wiley, 1999.
- [62] G. Mie, “Beiträge zur Optik trüber Medien, speziell kolloidaler Metallösungen,” *Ann. Phys. (Berlin)*, vol. 330, no. 3, pp. 377–445, 1908.
- [63] H. Kuwata, H. Tamaru, K. Esumi, and K. Miyano, “Resonant light scattering from metal nanoparticles: practical analysis beyond the Rayleigh approximation,” *Appl. Phys. Lett.*, vol. 83, no. 22, pp. 4625–4627, 2003.
- [64] E. Saydanzad, J. Li, and U. Thumm, “Characterization of induced nanoplasmonic fields in time-resolved photoemission: a classical trajectory approach applied to gold nanospheres,” *Phys. Rev. A*, vol. 95, no. 5, p. 053406, 2017.
- [65] W. M. Haynes, *CRC Handbook of Chemistry and Physics*, Boca Raton, CRC Press, 2014.
- [66] R. Howard Fowler and L. Nordheim, “Electron emission in intense electric fields,” *Proceedings of the Royal Society of London. Series A*, vol. 119, no. 781, pp. 173–181, 1928.
- [67] U. Thumm, “Hollow ion formation and decay in slow Bi^{46+} - C_{60} collisions,” *Phys. Rev. A*, vol. 55, no. 1, pp. 479–487, 1997.
- [68] U. Thumm, A. Bárány, H. Cederquist, L. Hägg, and C. J. Setterlind, “Energy gain in collisions of highly charged ions with C_{60} ,” *Phys. Rev. A*, vol. 56, no. 6, pp. 4799–4806, 1997.
- [69] B. Walch, U. Thumm, M. Stöckli, C. L. Cocke, and S. Klawikowski, “Angular distributions of projectiles following electron capture from C_{60} by 2.5-keV Ar^{8+} ,” *Phys. Rev. A*, vol. 58, no. 2, pp. 1261–1266, 1998.
- [70] M. Krüger, M. Schenk, P. Hommelhoff, G. Wachter, C. Lemell, and J. Burgdörfer, “Interaction of ultrashort laser pulses with metal nanotips: a model system for strong-field phenomena,” *New J. Phys.*, vol. 14, no. 8, p. 085019, 2012.
- [71] M. Schenk, M. Krüger, and P. Hommelhoff, “Strong-field above-threshold photoemission from sharp metal tips,” *Phys. Rev. Lett.*, vol. 105, no. 25, p. 257601, 2010.
- [72] W. C. Wallace, *et al.*, “Precise and accurate measurements of strong-field photoionization and a transferable laser intensity calibration standard,” *Phys. Rev. Lett.*, vol. 117, no. 5, p. 053001, 2016.

Supplementary Material

S1 Intensity-dependent VMI spectra for 100 nm silver nanospheres

Figure S1 shows simulated and experimental VMI spectra for 100 nm diameter silver nanospheres.

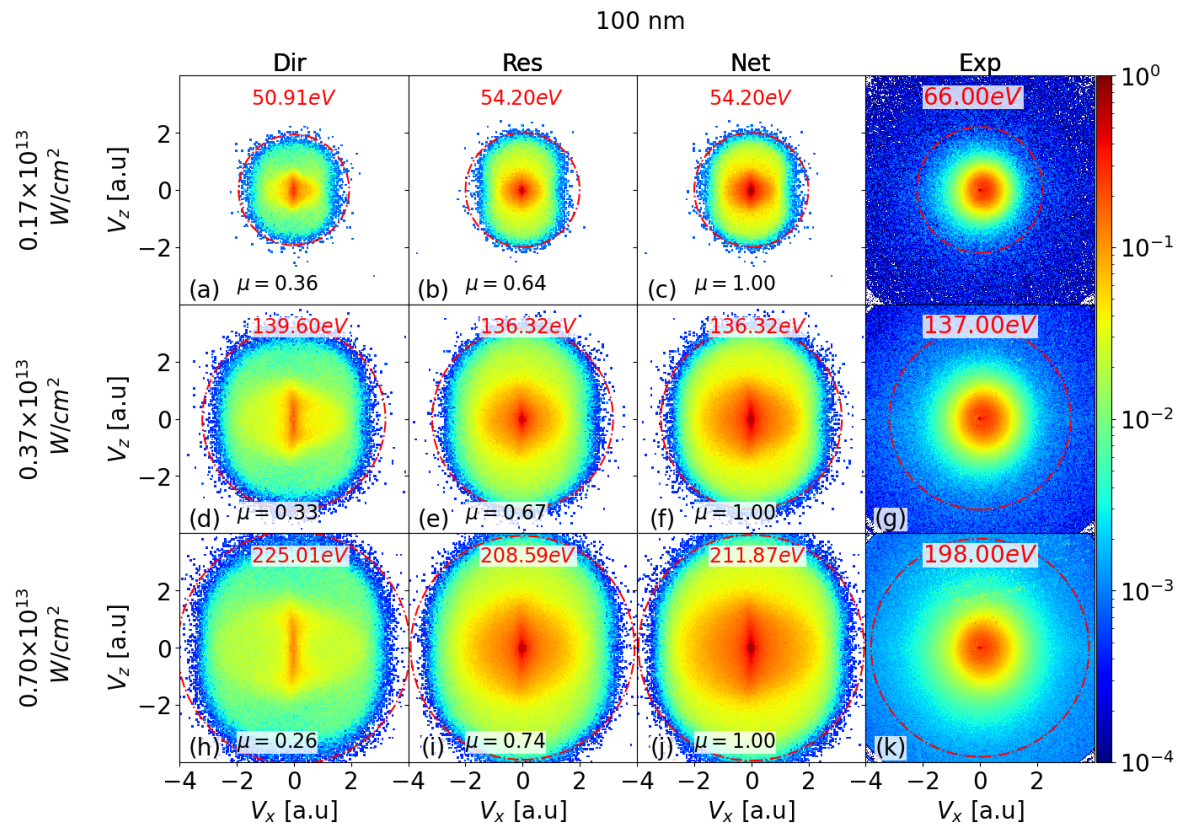


Fig. S1: As Fig. 2 in the main text for 100 nm diameter silver nanospheres and laser peak intensities of 1.7×10^{12} , 3.7×10^{12} , and 7.0×10^{12} W/cm^2 (first - third row, respectively). The laser-pulse length and wavelength are 25 fs and 780 nm. In each row, μ is the integrated PE yield, normalized to the integrated net yield in the third column. The red circle on each VMI map represents the cutoff. The value of the cutoff energy is displayed in red above each VMI graph.

S2 Intensity- and size-dependent VMI spectra for gold nanospheres

Figures S2, S3, and S4 show simulated VMI spectra for Au nanospheres with diameters of 10, 60, and 100 nm respectively.

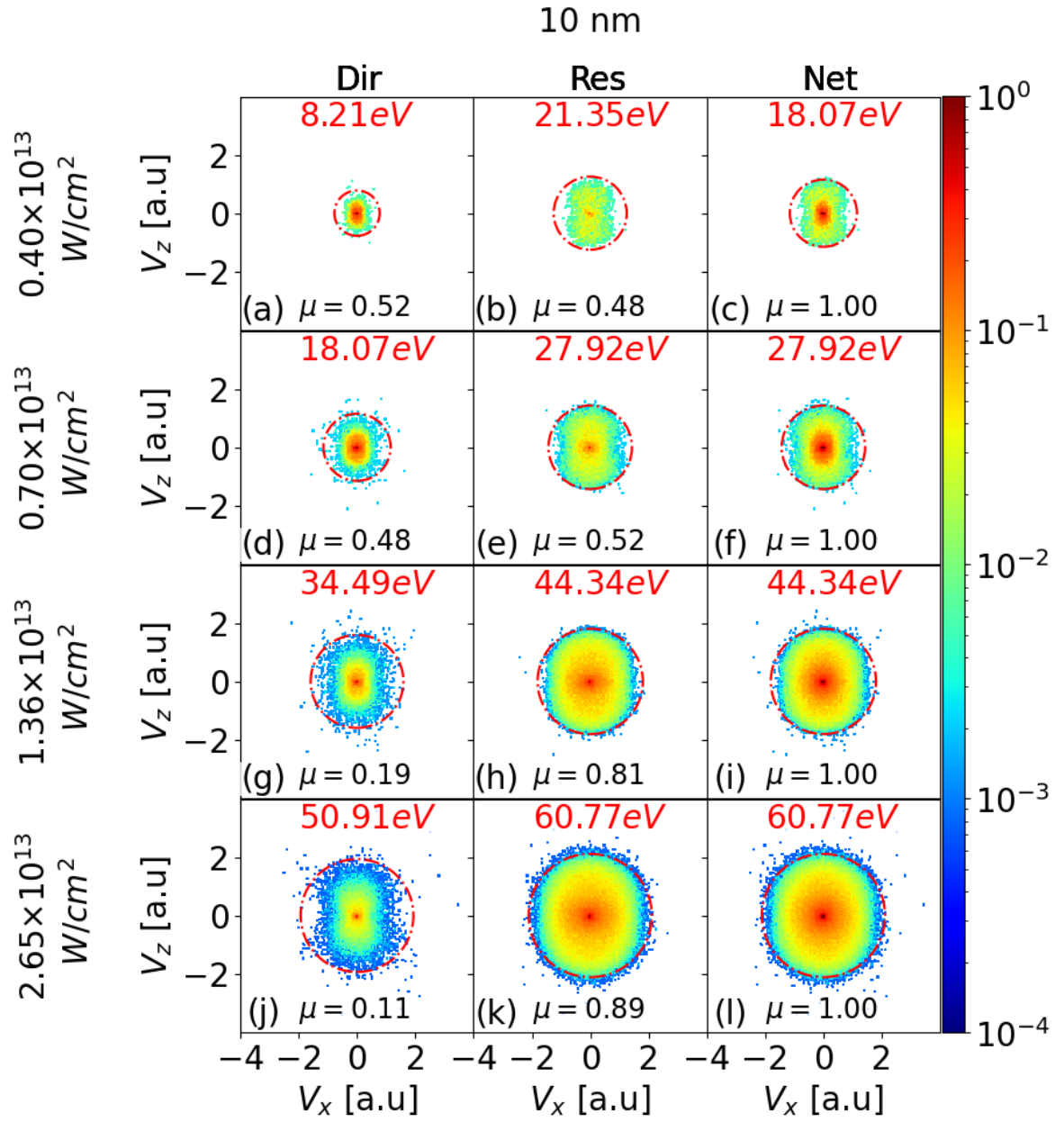


Fig. S2: As the numerical results in Fig. 2 in the main text for gold nanospheres.

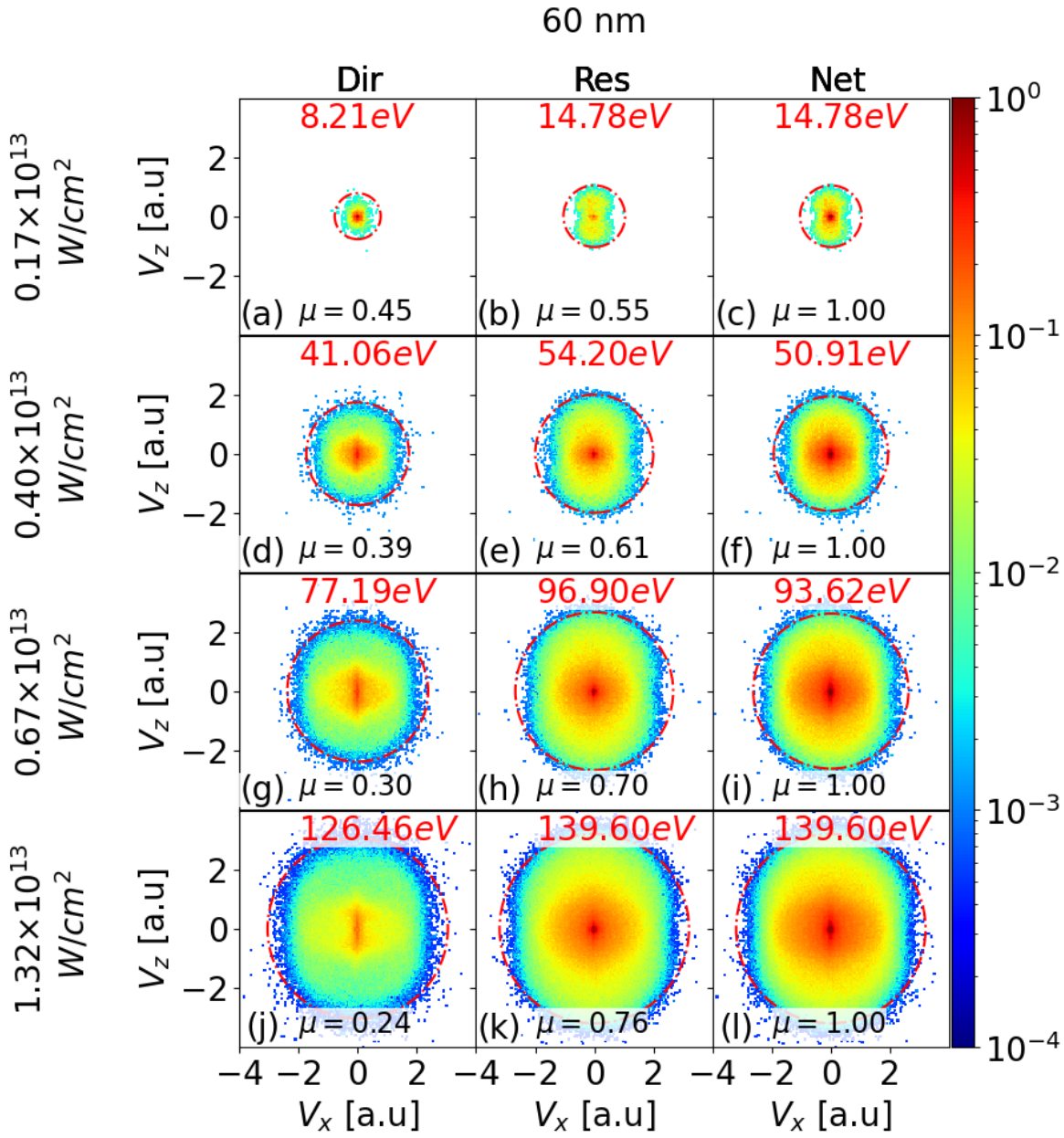


Fig. S3: As the numerical results in Fig. 3 in the main text for gold nanoparticles

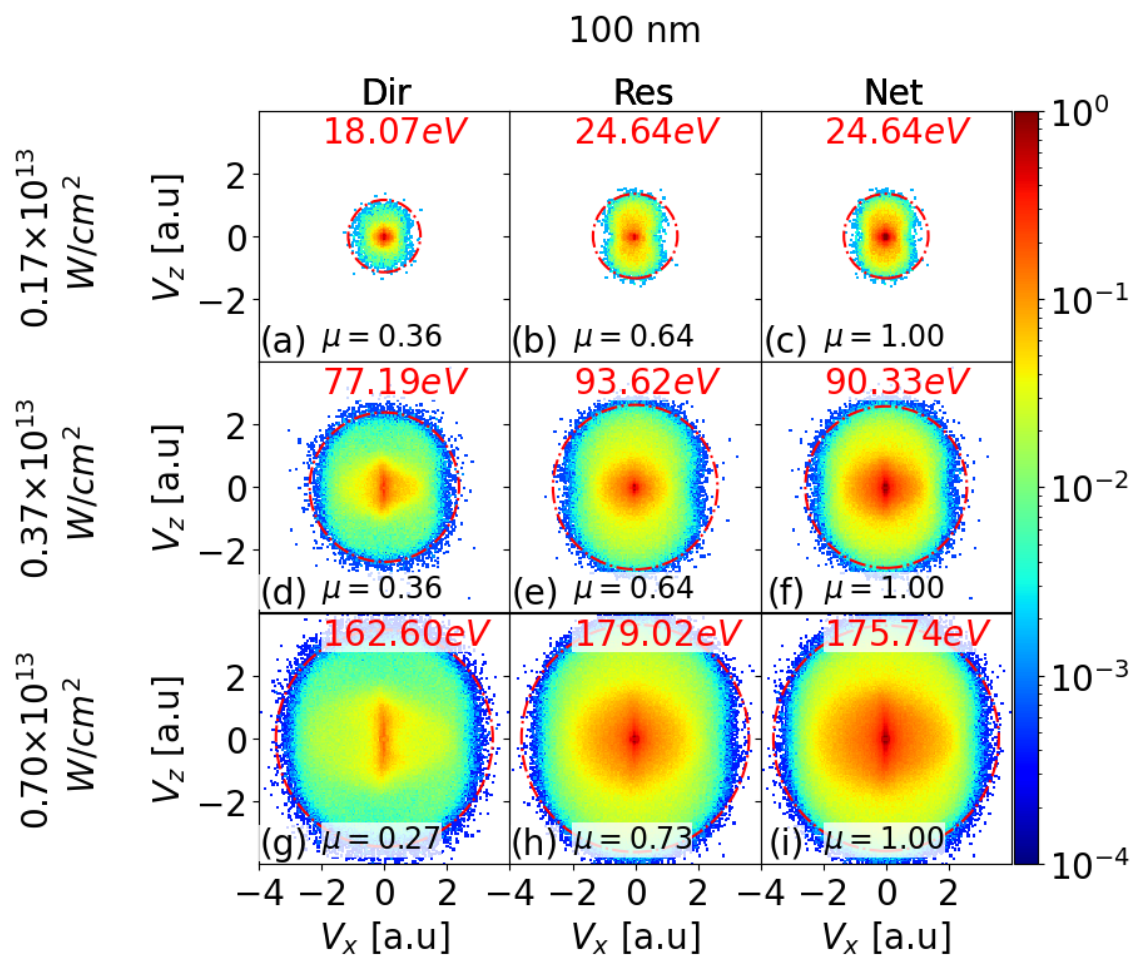


Fig. S4: As the numerical results in Fig. S1 in the main text for gold nanospheres

Figure S5 shows simulated and experimental VMI spectra for gold NPs with a diameter of 70 nm.

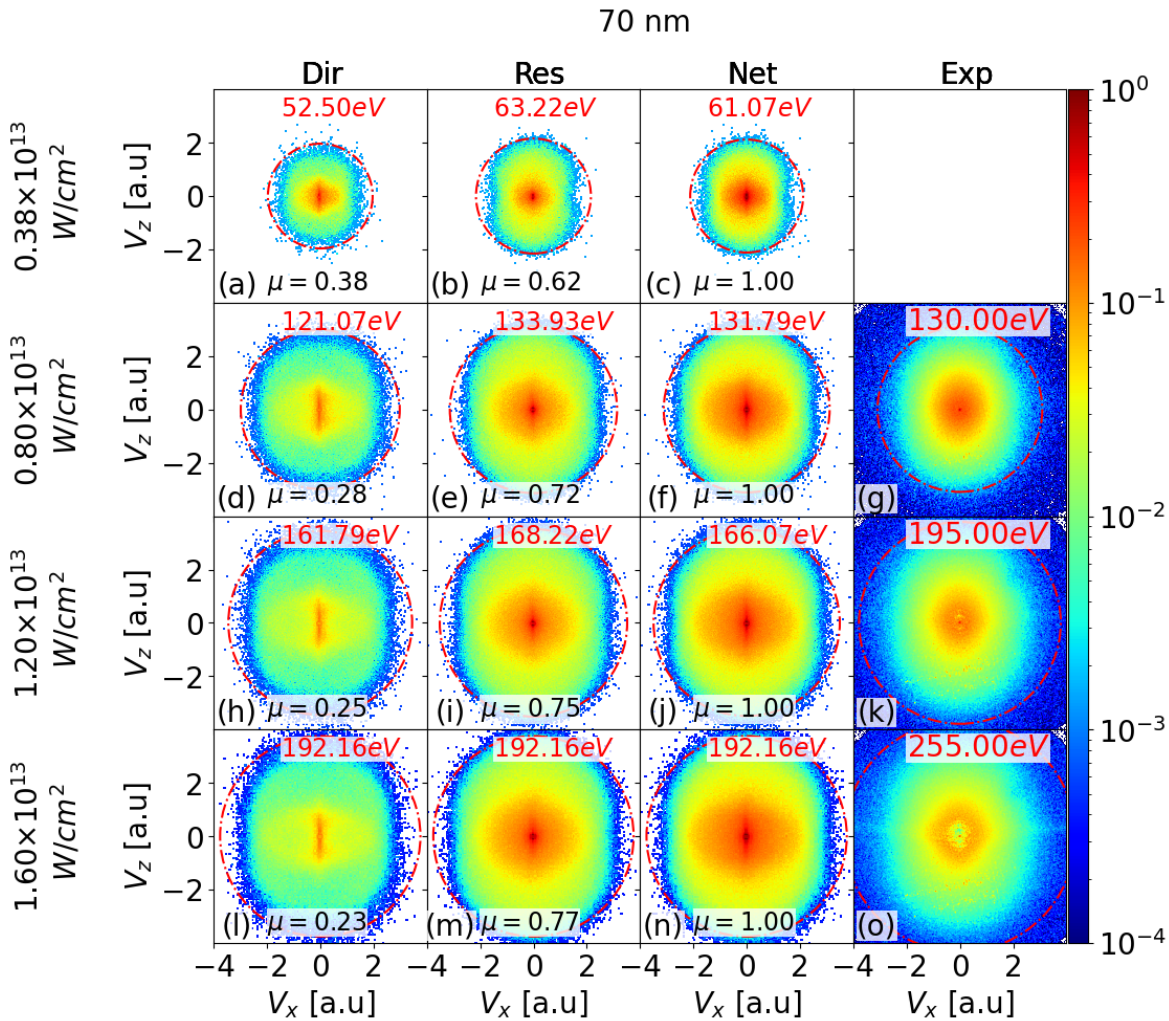


Fig. S5: Comparison of simulated direct (first column), rescattered (second column) and net (i.e., including direct and rescattered yields, third column) PE VMI spectra for gold nanospheres with a diameter of 70 nm and laser peak intensities of $I_0 = 3.8 \times 10^{12}$, 8.0×10^{12} , 1.2×10^{13} , and 1.6×10^{13} W/cm^2 (first - forth row, respectively).

S3 Intensity- and size-dependent VMI spectra for platinum nanospheres

Figure S6 shows simulated and experimental VMI spectra for platinum nanospheres with a diameter of 70 nm.

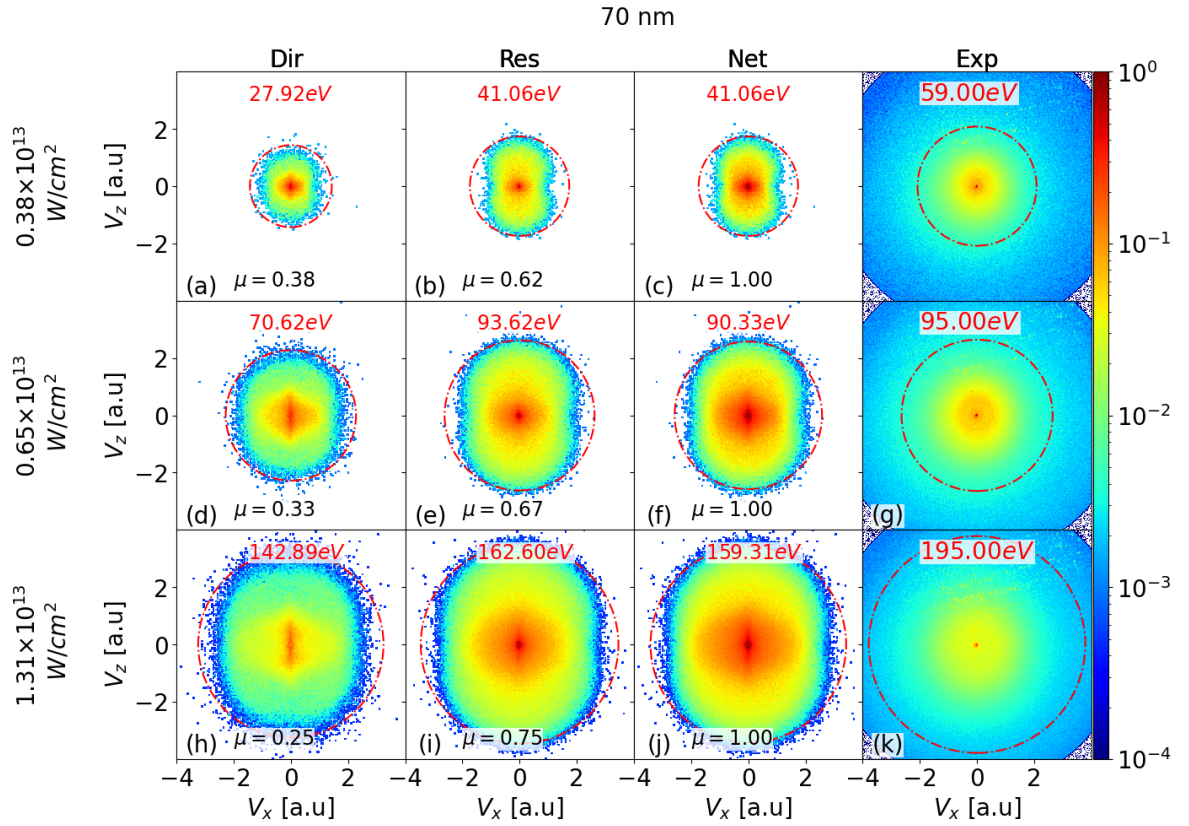


Fig. S6: Comparison of simulated direct (first column), rescattered (second column), and net (i.e., including direct and rescattered yields, third column) PE VMI spectra for platinum nanoparticles with a diameter of 70 nm and laser peak intensities of $I_0 = 3.8 \times 10^{12}$, 6.5×10^{12} , and 1.31×10^{13} W/cm² (first - third row, respectively).